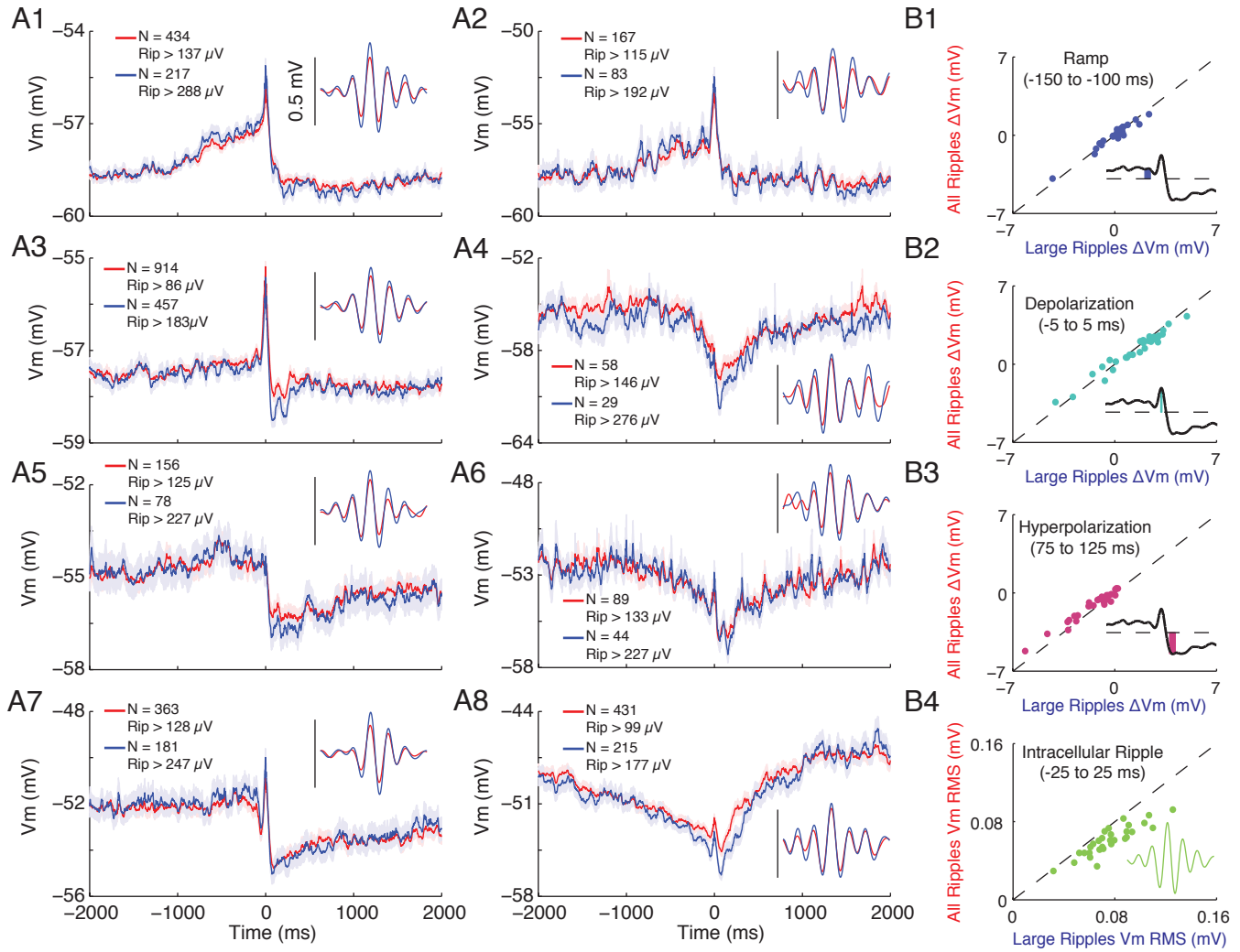


**Figure S1 (related to Figure 1). Membrane potential dynamics during single ripples are highly diverse**

**(A1)** Example of intracellular activity during four LFP ripples from a single neuron. LFPs from the four channels around the CA1 pyramidal cell layer are shown in black. The black dot marks the channel showing LFP ripples, which occur at time 0. The cyan dot marks the channel with LFP sharp waves. The membrane potential is shown in red below. Note that while ripples are readily detected in the LFP, they are much less obvious in the membrane potential.

**(A2-3)** Same as in (A1) but for an additional two neurons.



**Figure S2 (related to Figure 2). The average membrane potential dynamics during ripples are robust with respect to LFP ripple detection criteria**

**(A1-A8)** Examples of ripple-triggered averages of the subthreshold  $V_m$  for individual neurons, as in Figure 2 C1-C8, but using more stringent (blue) or less stringent (red) ripple detection criteria. For each neuron, we detected LFP ripples greater than 4 times the median of the ripple-band envelope, resulting in 40% more ripples than in the main text. Shown in red is the average of all detected ripples. Shown in blue is the average of the largest half of ripples. Neurons are arranged according to their pre-ripple  $V_m$ . Shaded regions mark mean  $\pm$  SEM. Insets show the average intracellular ripple oscillation for all ripples (red) and the largest half (blue), from -25 to 25 ms. Each legend lists the number of ripples entering the averages and LFP ripple detection threshold. Note that the shape of the average membrane potential is very similar for both low and high detection thresholds, suggesting that the observed neuron-to-neuron diversity is not a result of different detection thresholds.

**(B1)** Correlation between the amplitude of the ramp using more stringent (x-axis) and less stringent (y-axis) ripple detection criteria. Each dot is a neuron. Note that most neurons lie along the diagonal, indicating that the amplitude of the ramp is similar, independent of ripple detection threshold.

**(B2)** Same as in B1, but for the amplitude of the depolarization.

**(B3)** Same as in B1, but for the amplitude of the hyperpolarization.

**(B4)** Same as in B1, but for the amplitude of the intracellular ripple oscillation.

Note, all amplitudes are computed as in Figures 2/3.

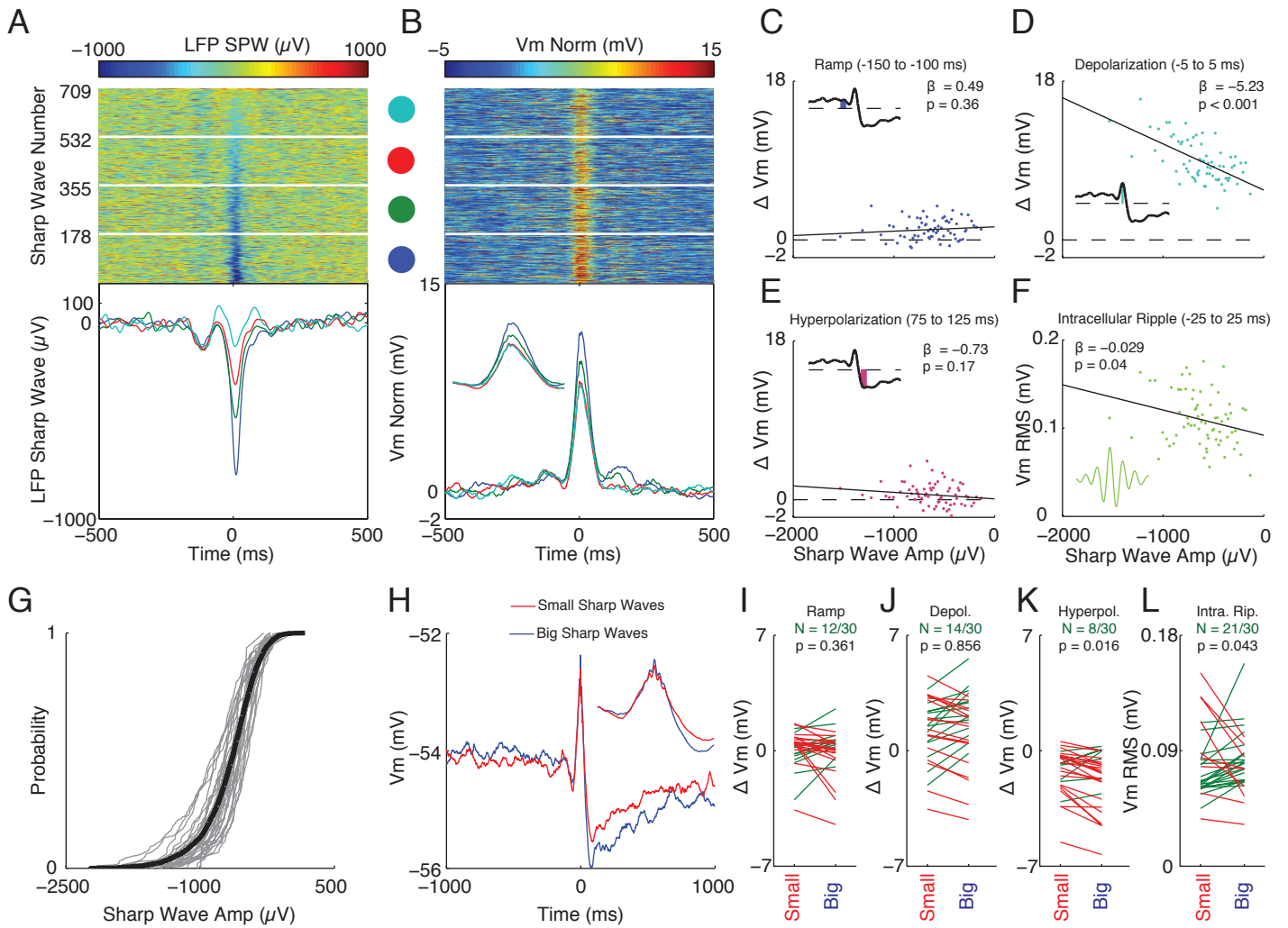


**Figure S3 (related to Figure 4) The intracellular depolarization scales with LFP sharp wave amplitude under hyperpolarizing current injection**

**(A)** Top: Ripple-triggered LFP from stratum radiatum sorted by sharp wave amplitude for all 709 ripples during hyperpolarizing current injection ( $N=10$  neurons). Bottom: Quartile averages color coded according to dots above.

**(B)** Top: Subthreshold Vm sorted by sharp wave amplitude from (A). Each row is normalized to have 0 mean (Vm Norm). Quartile averages shown below. The inset shows a magnified view of the depolarization ( $\pm 100$  ms). Note that, under hyperpolarizing current injection, which decreases the driving force for inhibition, larger sharp waves are associated with a larger intracellular depolarization, which further supports the notion that sharp wave amplitude correlates with net excitatory current. It also provides further support for the conceptual model in Figure S7.

**(C)** Scatter plot between LFP sharp wave amplitude and intracellular ramp amplitude. For C-F, the sharp wave sorted response matrices (from A-B) were divided into 70 blocked averages of 10 sharp waves each, and the amplitude of each component was computed as in Figures 2-3. The inset shows a schematic of how ramp amplitude was computed.

**(D)** Same as in C, but for the amplitude of the depolarization.

**(E)** Same as in C, but for the amplitude of the hyperpolarization.

**(F)** Same as in C, but for the amplitude of the intracellular ripple.

**(G)** Cumulative distribution function (CDF) of each neuron's LFP sharp wave amplitudes (grey). The CDF for all sharp waves is shown in black.

**(H)** Grand average of the subthreshold Vm from the smallest (red) and largest (blue) half of sharp waves, averaged across neurons. For each neuron, the ripple-triggered subthreshold Vm was sorted by the amplitude of the neuron's LFP sharp waves and broken into two averages: one from the smallest half and one from the largest half of sharp waves. The amplitudes of the four intracellular components from these two averages are compared in (I-L) for all 30 neurons. This procedure controls for differences in sharp wave amplitude across neurons. Note that only the post-ripple hyperpolarization shows an obvious modulation with sharp wave amplitude, consistent with grouped data from Figure 4.

**(I)** The intracellular ramp amplitude is plotted for the smallest and largest half of LFP sharp waves for all 30 neurons. Neurons whose ramp amplitude was more hyperpolarized for big sharp waves are shown in red. Neurons whose ramp amplitude is more depolarized for big sharp waves are shown in green. The number of neurons with more depolarized ramps with big sharp waves is reported in the inset above, along with a p-value testing whether the proportion of neurons is significantly different expected proportion of 0.5 using a two-sided binomial test.

**(J)** Same as in (I), but for the amplitude of the depolarization. Note that about as many neurons show larger depolarizations with big sharp waves as show smaller depolarizations, consistent with a balance of excitation and inhibition across neurons.

**(K)** Same as in (I), but for the amplitude of the hyperpolarization. Note that a significant majority of neurons show larger hyperpolarizations for big sharp waves.

**(L)** Same as in (I), but for the amplitude of the intracellular ripple oscillation. Note that a significant majority of neurons show larger intracellular ripple oscillations with big sharp waves.

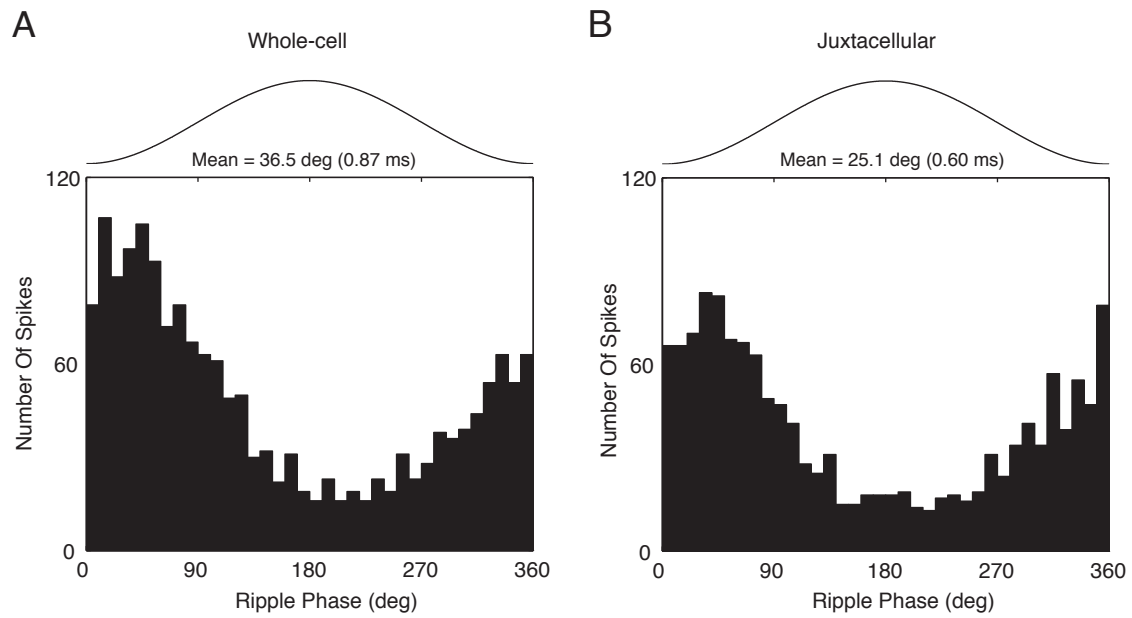


**Figure S4 (related to Figure 5). Spikes are phase-locked near the trough of LFP ripple oscillations**

**(A)** Distribution of spike phases relative to the LFP ripple oscillation from whole-cell recordings.

**(B)** Same as in (A), but for N=28 putative CA1 pyramidal neurons from juxtacellular recordings in the same mice used for whole-cell recordings.

Note that for both whole-cell and juxtacellular recordings, spikes occur ~0.8 ms after the trough of LFP ripple oscillations.

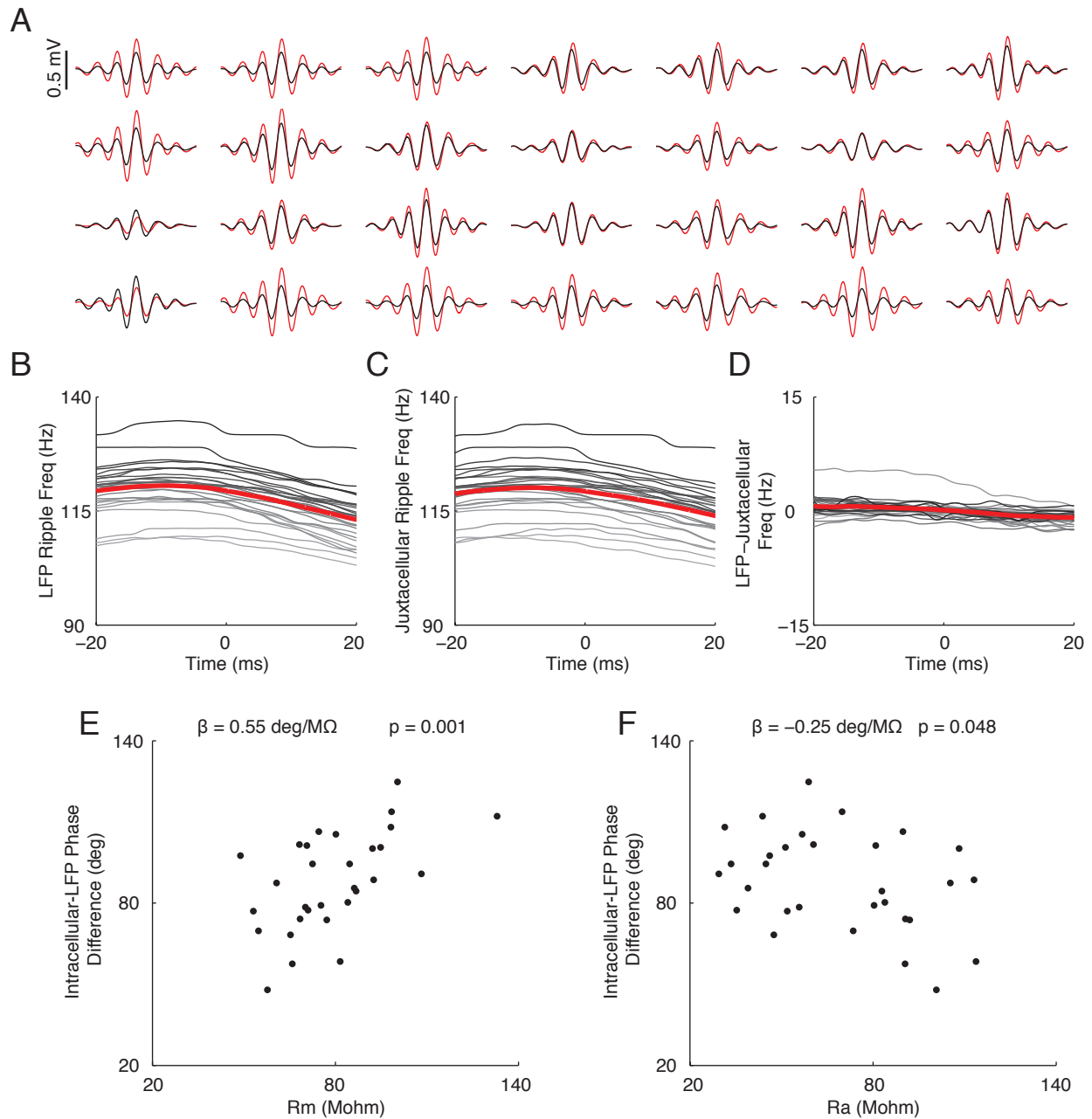


**Figure S5 (related to Figure 6). Juxtacellular LFP ripples are synchronous with probe LFP ripples. Relationship between input and access resistance and the intracellular-LFP ripple phase difference**

**(A)** Each juxtacellular recording's average LFP ripple (red) and the probe's LFP ripple (black) from -25 to 25 ms. For all recordings, juxtacellular LFP ripples were recorded from the same anatomical location where whole-cell recordings were performed. Note that juxtacellular ripples and ripples recorded from probe are nearly synchronous.

**(B)** Instantaneous LFP ripple frequency recorded on extracellular probe. For B-D, each recording's average is grey scaled according to its probe LFP ripple frequency at time 0. Averages are shown in red.

**(C)** Same as in B, but for juxtacellular LFP ripples.

**(D)** Same as in B, but showing the difference between probe LFP and juxtacellular ripple frequency. Notice that ripples recorded on the extracellular multisite probe and juxtacellularly on a pipette are very similar, in contrast to the differences observed in the whole-cell recordings.

**(E)** Scatter plot of each neuron's input resistance ( $R_m$ ) and phase delay between its intracellular ripples and LFP ripples.

**(F)** Scatter plot of each neuron's access resistance ( $R_a$ ) and the intracellular-LFP ripple phase delay.

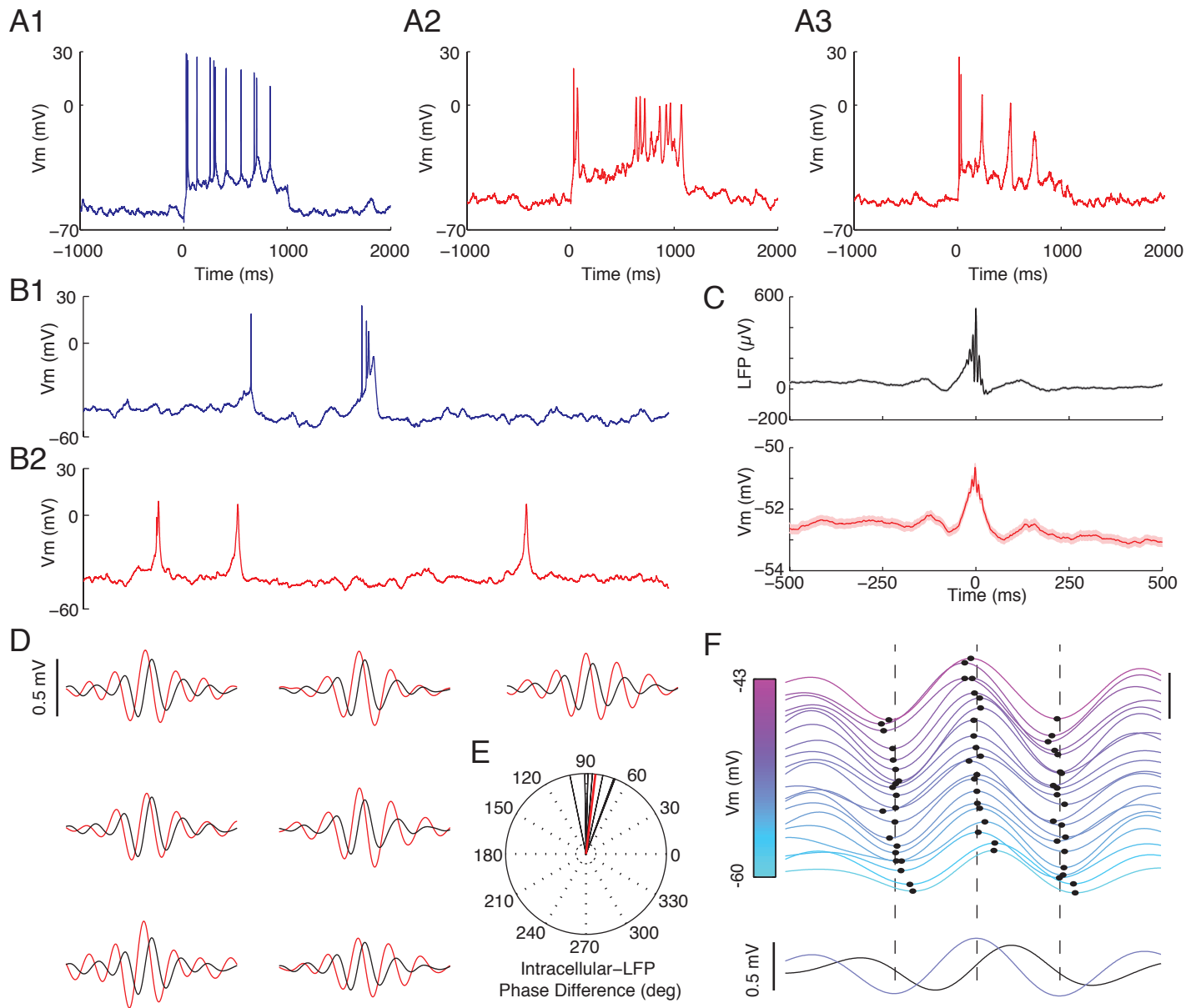


**Figure S6 (related to Figure 7). Intracellular blockade of voltage-gated sodium channels using QX-314 has no effect on intracellular ripple oscillations**

**(A1)** Example of an intracellular response to a 1-second depolarizing current step, immediately after breaking into the neuron. Note the presence of large sodium spikes of attenuating amplitude.

**(A2-A3)** Same as in (A1), but a couple minutes after breaking into a neuron. While depolarizing current occasionally evoked 1-2 sodium spikes immediately after the start of the pulse, sodium spikes were largely replaced with slower, putative calcium spikes.

**(B1)** Three second example of spontaneous activity immediately after breaking into the neuron. Note the presence of a single sodium spike and a complex burst.

**(B2)** Same as in (B1), but after full QX-314 wash in. Note that sodium spikes have been replaced with slower, putative calcium spikes, similar to previous reports (Grienberger et al., 2014). Combined with the intracellular current steps, this demonstrates the effectiveness of QX-314 in blocking voltage-gated sodium channels.

**(C)** Ripple-triggered averages of the LFP from the CA1 pyramidal cell layer (top) and subthreshold Vm (bottom) for 1070 ripples recorded from 7 neurons with intracellular QX-314. Shaded regions mark mean  $\pm$  SEM. Note that while the intracellular depolarization and ripple oscillations are largely unaffected, the post-ripple hyperpolarization is diminished, consistent with the ability of QX-314 to block GABA<sub>B</sub>-mediated conductances.

**(D)** Each neuron's average intracellular ripple (red) and LFP ripple (black) from -25 to 25 ms around LFP ripple center. Note that for all neurons the central peak in the LFP lags behind the central peak in the Vm, as in drug-free neurons (Figure 6).

**(E)** Intracellular-LFP ripple phase difference (at time 0) for all 7 neurons (black lines). Average shown in red. Note that intracellular ripples lead LFP ripples by  $\sim 90$  degrees, similar to drug-free neurons (Figure 6). If voltage-gated sodium contributed to intracellular ripples around resting Vm, then blocking them should have shifted the intracellular-LFP ripple phase difference.

**(F)** Top: Average intracellular ripple (from -8 to 12 ms) plotted as a function of Vm for the range of spontaneous Vm fluctuations. All ripples lacking intracellular action potentials were sorted by their peri-ripple Vm ( $\pm 25$  ms average), and 21 averages of 50 ripples each are displayed. Traces are separated by 0.1 mV (scale bar in upper right is 0.5 mV) and colored according to their peri-ripple Vm. The central peak and the preceding/subsequent troughs are marked by black dots for each trace. Vertical bars mark average time of preceding trough, central peak, and subsequent trough. Note that hyperpolarized ripples (cyan) are phase delayed relative to depolarized ripples (pink). Bottom: Average LFP ripple (black) and intracellular ripple (light blue). Note that the voltage dependence of intracellular ripple phase in QX-314 neurons is almost identical to drug-free neurons (Figure 7), which further demonstrates that voltage-gated sodium channels do not appreciably contribute to intracellular ripple oscillations.

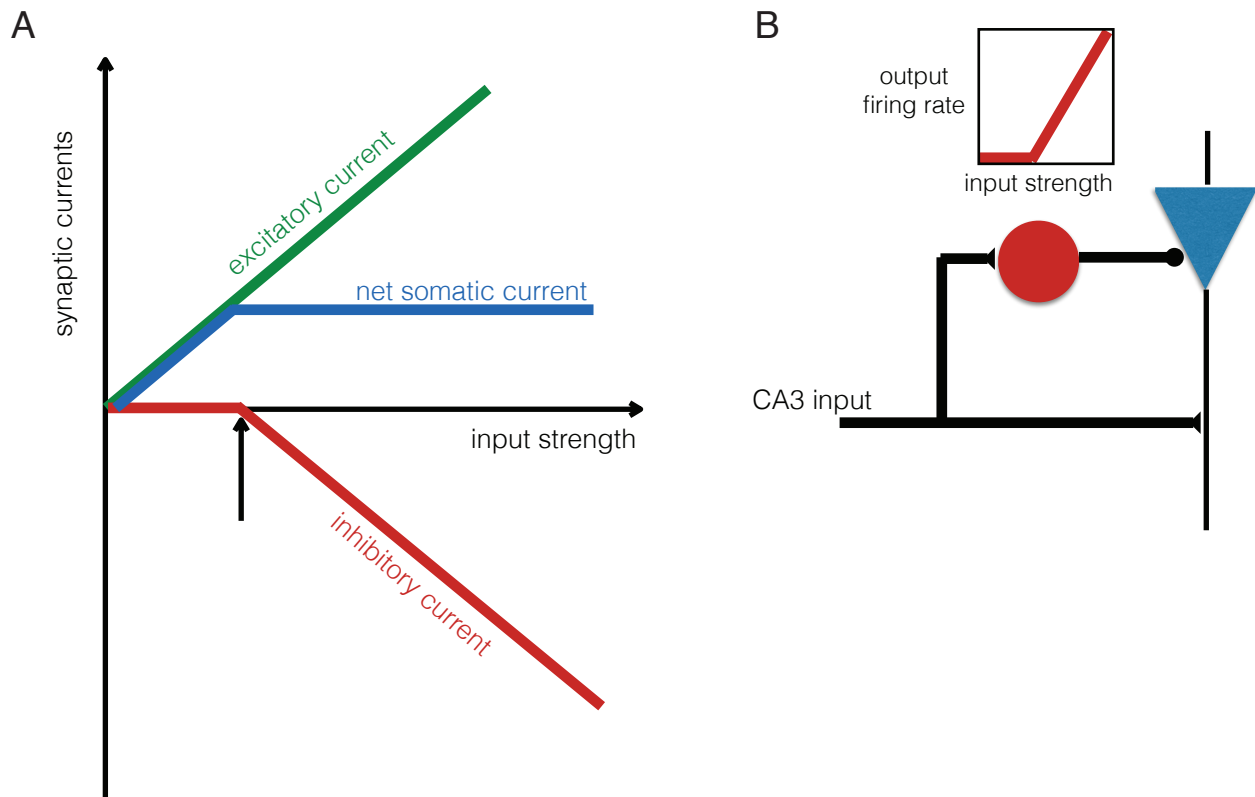


**Figure S7 (related to Figure 4). Conceptual model explaining a potential mechanism balancing excitation and inhibition as a function of CA3 input strength**

**(A)** The amplitude of the net excitatory current from direct CA3 input (green), the amplitude of feed-forward inhibition through local CA1 interneurons (red), and the total net somatic current driving CA1 pyramidal neurons (blue) are plotted as a function of CA3 input strength, as assessed experimentally using the amplitude of LFP sharp waves. Due to direct excitatory input, the amplitude of excitatory current grows linearly with input strength. Due to the fact that weak CA3 inputs won't bring CA1 interneurons to spike threshold, their output is constant up to a threshold (arrow), and grows at the same rate as excitation beyond this point. The combination of such direct excitation and indirect inhibition ensures that the total somatic current is constant above a certain threshold. Ripples are hypothesized to occur in this range, under strong input strengths. This mechanism can potentially explain why the amplitude of the intracellular depolarization is independent of input strength on average. In contrast, for a neuron to fire during a given ripple, it must receive an excitation that is much greater than the average excitation shown in green.

**(B)** Diagram showing direct excitatory input onto a CA1 pyramidal neuron (blue) with feed-forward inhibition through a local CA1 interneuron (red). The output firing rate of the local CA1 interneuron is constant below a certain threshold, and grows linearly above this threshold.



## **Supplemental Experimental Procedures:**

All animal procedures were performed in accordance with National Institute of Health guidelines and with approval of the Caltech Institutional Animal Care and Use Committee.

### **Head fixation surgery:**

Sixteen male C57Bl/6 mice (Charles River Laboratories) were surgically implanted with a light-weight, stainless steel ring embedded in dental cement, which allowed for mechanically stable head-fixation in the recording apparatus, as previously described (Froudarakis et al., 2014). A stainless steel wire was implanted over the right cerebellum. The skull was leveled and the locations of the pipette (-1.9 mm posterior, 1.5 mm lateral from Bregma) and probe exposures (-1.7 mm posterior, 2.0 mm lateral from Bregma) were marked on the skull over the left hemisphere. Following surgery, mice were returned to their home cage, maintained on a 12 hour light/dark cycle, and given access to food and water *ad libitum*. Ibuprofen (0.2 mg/mL) was added to the water as a long-term analgesic. Mice were given at least 48 hours to recover before the day of the experiment.

### **Exposure surgery**

On the day of the experiment, mice (age P28 to P37) first underwent a short surgery to expose the brain. While anesthetized with 1% isoflurane and head-fixed in the stereotaxic apparatus, two small exposures were drilled (pipette: 500  $\mu$ m diameter; probe: 200  $\mu$ m diameter) over the left hippocampus at the previously marked locations. A recording chamber was secured on top of the head-fixation device and filled with pre-oxygenated (95% O<sub>2</sub>, 5% CO<sub>2</sub>), filtered (0.22  $\mu$ m) artificial cerebrospinal fluid (aCSF) containing (in mM): 125 NaCl, 26.2 NaHCO<sub>3</sub>, 10 Dextrose, 2.5 KCl, 2.5 CaCl<sub>2</sub>, 1.3 MgSO<sub>4</sub>, 1.0 NaH<sub>2</sub>PO<sub>4</sub>.

### **Awake, *in vivo* recordings**

Mice were head-fixed on top of a spherical treadmill secured on an air table (TMC). The ball could rotate along a single axis, allowing the mice to run and walk freely. On either side of the ball, two platforms supporting micromanipulators (Sutter Instrument Company) allowed for precise positioning of a silicon probe (mouse's left) and glass pipettes (mouse's right). A single-shank, 32-site silicon probe (NeuroNexus) with 100  $\mu$ m site spacing was inserted in the coronal plane (~15 degree angle pointing towards the midline) to a depth of 2600-3000  $\mu$ m. Sites spanned all of neocortex, area CA1, the dentate gyrus, and parts of the thalamus. The probe was adjusted so that a recording site was positioned within the CA1 pyramidal cell layer for reliably recording LFP ripple oscillations. Sharp waves were evident on the sites spanning *stratum radiatum*. The probes were grounded to the recording table and referenced to a wire implanted over the cerebellum.

To find the depth of the CA1 cell layer and compare the structure of LFP ripples recorded on the probe versus those from a pipette, we used artificial cerebrospinal fluid (aCSF) filled pipettes to perform one to three juxtacellular (Pinault, 1996) recordings per mouse from putative CA1 pyramidal neurons (N=28). Long-taper pipettes (for juxtacellular and whole-cell recordings) were pulled from borosilicate capillaries (OD: 1.0 mm, ID: 0.58 mm; Sutter Instrument Company) using a Model P-2000 puller (Sutter Instrument Company) to an inner tip diameter of ~0.8-1.5  $\mu$ m and outer diameter of ~2  $\mu$ m (5-8 M $\Omega$ ), and inserted into the brain in the coronal plane with a ~15 degree angle pointing away from the midline. The location of the CA1 layer was signaled by the occurrence of large amplitude ripples that appeared synchronously on the pipette and probe site in the CA1 cell layer. At the depth of the CA1 layer, the probe and patch pipette were separated by approximately 200  $\mu$ m in the anterior-posterior direction and 100  $\mu$ m in the medial-lateral. The pipette was advanced at 1-2  $\mu$ m/s until a putative CA1 pyramidal neuron was encountered, which was evident from the appearance of complex spikes and ripple-associated action potentials. Recordings (juxtacellular and whole-cell) were made with a MultiClamp 700B amplifier



(Molecular Devices). For juxtacellular recordings, the capacitance neutralization circuit was off and the output was AC coupled and amplified 100x.

Whole-cell recordings were performed after the depth of the CA1 layer had been identified. Pipettes were filled with an internal solution containing (in mM): 115 K-Gluconate, 10 KCl, 10 NaCl, 10 Hepes, 0.1 EGTA, 10 Tris-phosphocreatine, 5 KOH, 13.4 Biocytin, 5 Mg-ATP, 0.3 Tris-GTP. The internal solution had an osmolarity of 300 mOsm and a pH of 7.27 at room temperature. In a subset of experiments (**Figure S6**), 2 mM of QX-314 (Tocris) was added to the internal solution to block voltage-gated sodium channels. The membrane potential was not corrected for the liquid junction potential. Whole-cell recordings were obtained “blind” according to previously described methods (Margrie et al., 2002) in current clamp mode (Schramm et al., 2014). Capacitance neutralization was set prior to establishing the GΩ seal. After obtaining the whole-cell configuration, the neuron’s membrane potential was recorded in current clamp mode. Access resistance was estimated online by fitting the voltage response to hyperpolarizing current steps (see below). Recordings were aborted when the access resistance exceeded 120 MΩ or the action potential peak dropped below 0 mV. One to five whole-cell recordings (N=37) were performed per mouse.

#### Signal acquisition

All electrophysiological signal acquisition was performed with custom Labview software (National Instruments) that we developed. Electrophysiological signals were sampled simultaneously at 25 kHz with 24 bit resolution using AC (PXI-4498, internal gain: 30 dB, range: +/- 316 mV) or DC-coupled (PXIe-4492, internal gain: 0 dB, range: +/- 10 V) analog-to-digital data acquisition cards (National instruments) with built-in anti-aliasing filters for extracellular and intracellular/juxtacellular recordings, respectively.

#### Histology and imaging:

Following the experiment, mice were deeply anesthetized with 5% isoflurane, decapitated, and the brain extracted to 4% PFA. Staining of biocytin-filled cells for morphological identification was performed according to previously described methods (Horikawa and Armstrong, 1988). Brains were fixed at 4° C in 4% paraformaldehyde overnight and transferred to 0.01 M (300 mOsm) phosphate buffered saline (PBS) the next day. Up to one week later, brains were sectioned coronally (100 μm) on a vibrating microtome (Leica), permeabilized with 1% Triton X-100 (v/v) in PBS for 1-2 h, and incubated overnight at room temperature in PBS containing avidin-fluorescein (1:200, Vector Laboratories), 5% (v/v) normal horse serum (NHS), and 0.1% Triton X-100. Sections were rinsed in PBS between each step. The next day, sections containing biocytin stained neurons were identified on an inverted epifluorescent microscope (Olympus IX51) for further immunohistochemical processing.

To aid in classifying recorded neurons as CA1 pyramidal neurons, we performed immunohistochemical staining against calbindin (CB) and parvalbumin (PV). Sections containing biocytin-stained neurons were first incubated in blocking solution containing 5% NHS, 0.25% Triton X-100, and 0.02% (wt/v) sodium azide in PBS. Next, slices were incubated in PBS containing primary antibodies against CB (Rabbit anti-Calbindin D-28k, 1:2000, Swant) and PV (Goat anti-parvalbumin, 1:2000, Swant) overnight. After thorough rinsing in PBS, slices were incubated in PBS containing secondary antibodies CF543 donkey anti-rabbit (1:500, Biotium) and CF633 donkey anti-goat (1:500, Biotium). Processed slices were rinsed and mounted in antifading mounting medium (EverBrite, Biotium).

Stained slices were imaged on an inverted confocal laser-scanning microscope (LSM 710, Zeiss). Biocytin-stained neurons were unambiguously classified as CA1 pyramidal neurons if their soma was located in the CA1 pyramidal cell layer, showed a morphology characteristic of these neurons (bifurcating apical dendrites, dendritic spines, etc.), had PV-negative soma, and showed electrophysiological properties consistent with CA1 pyramidal neurons.

### Measuring and setting access resistance

Access resistance was estimated online using custom-written software in Labview that communicated with the software (Commander, Molecular Devices) controlling the MultiClamp 700B amplifier through an application programming interface (API). To estimate the access resistance, the bridge balance was temporarily turned off. Then, two -100 pA current pulses (250 ms duration, 250 ms inter-pulse interval) were delivered, the first 50 ms of the hyperpolarizing voltage responses was fit using a simple model, and if the  $r^2$  fit exceeds 0.99, the bridge balance was set to its new value, otherwise it was returned to the previous value. This procedure was performed once every minute during whole-cell recordings. In addition, all recording parameters in the Commander software were acquired once every second using the API, time stamped to electrophysiological signals, and saved for offline review. The pipette's voltage response to hyperpolarizing current steps was fit online using a simple double exponential model (Anderson et al., 2000). The computational simplicity of this model sped online fitting. For offline estimates, we used a biophysically-inspired, single-compartment model (de Sa and MacKay, 2001). The results obtained from the two models were nearly identical under our recording conditions.

### Ripple detection

All offline analysis was performed in Matlab (MathWorks). LFP ripple oscillations were detected as transient increases in ripple-band power from the probe site located in the CA1 pyramidal cell layer. To compute ripple band power, LFPs were filtered between 80-180 Hz (Parks-McClellan optimal equiripple FIR filter, 80-180 Hz pass band, 50-80 and 180-200 Hz transition bands, 60 dB minimum attenuation in the stop bands), the ripple-band envelope was computed as the instantaneous amplitude from the Hilbert transform, and the envelope was low-pass filtered (Parks-McClellan optimal equiripple FIR filter, 20-30 Hz transition band, 40 dB minimum attenuation in the stop bands). From this signal, an upper threshold was set as 4.5-5.5 times the median. A lower threshold was set as half the upper threshold. Ripples were detected as peaks in the ripple band envelope above the upper threshold, and with time between positive-going and negative-going lower threshold crossings longer than 30 ms. Ripples meeting these criteria, but with peaks less than 60 ms apart were merged. The time of ripple occurrence was defined as the sample with the largest amplitude (positive peak) in the ripple band within the detected ripple and used as time 0 for all plots (ripple center).

Having multiple extracellular recording sites aided in ripple detection for several reasons. First, it allowed us to precisely position a single LFP electrode in the CA1 pyramidal cell layer based on the well-known inversion of sharp wave polarity across the cell layer. Second, it allowed us to confirm that the detected ripples were localized to the CA1 pyramidal cell layer, which helps exclude electrical artifacts. Third, it enabled monitoring LFPs across the neocortex and hippocampal subfields to confirm that the whole network was in a healthy state, as established by previous multisite recordings.

### Quantification of intracellular and LFP waveforms

To quantify the intracellular response during ripples, we computed the change in subthreshold  $V_m$  relative to baseline in short time windows for the pre-ripple ramp (-150 to -100 ms), the sharp wave associated depolarization (-5 to 5 ms), and the post-ripple hyperpolarization (75 to 125 ms). The baseline  $V_m$  was subtracted from the median  $V_m$  in each component's time window to yield the component's amplitude. For neuron averaged (**Figure 2**) and block-averaged (**Figure 4**)  $V_m$  waveforms, the baseline  $V_m$  was defined as the average from -2 to -1.5 s. For intracellular ripples, the baseline was defined as the average  $V_m$  from -25 to 25 ms (**Figure 3**). To quantify the amplitude of intracellular ripple and LFP ripples, the root mean square of the ripple-band signal was computed from -25 to 25 ms.

The instantaneous phase, frequency, and power of juxtacellular, LFP, and intracellular ripples were measured using the continuous wavelet transform and complex Morlet wavelets with central

frequencies from 60 to 200 Hz in 0.025 Hz steps and a length of 5 cycles. For each sample, the frequency with the largest power was identified and its phase and frequency taken as the waveform's instantaneous value. For **Figure 6 B-E** and **Figure S5**, the instantaneous estimates were Gaussian smoothed ( $\sigma = 1$  ms). 8 neurons were excluded from **Figure 6 B-E** due to poor instantaneous estimates in the beginning or end of the  $\pm 20$  ms window, though this did not change the major results, as evidence from **Figure 6 F-H**, which includes all neurons.

#### Intracellular spike detection and subthreshold Vm calculation

Spikes from whole-cell recordings were detected as peaks greater than 10 mV after high-pass filtering the Vm (Parks-McClellan optimal equiripple FIR filter, 20-50 Hz transition band, 40 dB minimum attenuation in the stop bands). The subthreshold membrane potential was computed by linearly interpolating periods with action potentials from 3 ms before to 5 ms after the spike peak. For spikes occurring within 20 ms of each other, as during complex bursts, the first spike was linearly interpolated from 3 ms before its peak until the sample showing the minimum value before the next spike. This procedure provided a lower bound on complex spike waveforms, effectively revealing the slow, depolarizing component underlying them while excluding fast action potential waveforms (Epsztein et al., 2011). Following linear interpolation, the signals were low-pass filtered (Parks-McClellan optimal equiripple FIR filter, 250-350 Hz transition band, 40 dB minimum attenuation in the stop bands).

#### Juxtacellular spike detection

Juxtacellular spikes were detected as peaks greater than 0.25 mV after high-pass filtering (Parks-McClellan optimal equiripple FIR filter, 60-80 Hz transition band, 40 dB minimum attenuation in the stop bands). Single-unit isolation and stable spike waveform were confirmed offline.

#### Conductance-based Vm/LFP model

The conductance-based “ball-and-stick” model (**Figure 8 A**) was composed of a spherical perisomatic compartment with a radius of 10  $\mu\text{m}$  and cylindrical apical and basal dendritic compartments with 2  $\mu\text{m}$  radii and lengths of 50  $\mu\text{m}$ . 50  $\mu\text{m}$  separated the center of the perisomatic compartment and the center of the dendritic compartments, giving rise to an axial resistance of 2.8  $\text{M}\Omega$  (intracellular resistivity = 0.7  $\Omega\text{-m}$ ). Each compartment contained a resting conductance with a reversal potential of -55 mV and a magnitude given by the inverse of the product of its surface area and the specific membrane resistance (15  $\text{k}\Omega\text{-cm}^2$ ). Similarly, each compartment had a capacitance given by the product of its surface area and the specific membrane capacitance (1  $\mu\text{F}/\text{cm}^2$ ). Additionally, the perisomatic compartment had an excitatory synaptic conductance with a reversal potential of 10 mV and an inhibitory synaptic conductance with a reversal potential of -60 mV. These synaptic conductances served as the source of ripple-frequency (120 Hz) input to the model. To assess the dependence of intracellular ripple phase on Vm, the model was run at perisomatic Vm ranges from -150 to 50 mV in steps of 0.5 mV accomplished through DC current injection into the perisomatic compartment (**Figure 8 B1-B2**), as done experimentally (**Figure 7 C**). Using the model with zero DC current injection, the LFP at an electrode 50  $\mu\text{m}$  from the perisomatic compartment and equidistance from the dendritic compartments (ie in the middle of the “cell layer”) was calculated using the transmembrane currents from each compartment at each point in time. The extracellular space was assumed to be isotropic, uniform, and purely resistive (ohmic) with a resistivity of 0.333  $\Omega\text{-m}$ . The perisomatic compartment was approximated as a point source of current, while the dendritic compartments were approximated as line sources (Holt and Koch, 1999, Einevoll et al., 2013).

#### Supplemental References:

- Anderson, J. S., Carandini, M. & Ferster, D. (2000). Orientation tuning of input conductance, excitation, and inhibition in cat primary visual cortex. *J Neurophysiol.* 84, 909-26.
- de Sa, V. R. & MacKay, D. J. C. (2001). Model fitting as an aid to bridge balancing in neuronal recording. *Neurocomputing.* 38, 1651-1656.

- Einevoll, G. T., Kayser, C., Logothetis, N. K. & Panzeri, S. (2013). Modelling and analysis of local field potentials for studying the function of cortical circuits. *Nat Rev Neurosci.* 14, 770-85.
- Epszstein, J., Brecht, M. & Lee, A. K. (2011). Intracellular determinants of hippocampal CA1 place and silent cell activity in a novel environment. *Neuron.* 70, 109-20.
- Froudarakis, E., Berens, P., Ecker, A. S., Cotton, R. J., Sinz, F. H., Yatsenko, D., Saggau, P., Bethge, M. & Tolias, A. S. (2014). Population code in mouse V1 facilitates readout of natural scenes through increased sparseness. *Nat Neurosci.* 17, 851-7.
- Holt, G. R. & Koch, C. (1999). Electrical interactions via the extracellular potential near cell bodies. *J Comput Neurosci.* 6, 169-84.
- Horikawa, K. & Armstrong, W. E. (1988). A versatile means of intracellular labeling: injection of biocytin and its detection with avidin conjugates. *J Neurosci Methods.* 25, 1-11.
- Schramm, A. E., Marinazzo, D., Gener, T. & Graham, L. J. (2014). The Touch and Zap method for in vivo whole-cell patch recording of intrinsic and visual responses of cortical neurons and glial cells. *PLoS One.* 9, e97310.